the broadest features of its spatial pattern are in agreement with the GCM experiment.

The same GCM experiment (*10, 28*) produced significant negative sea-level pressure anomalies over continental Europe and North Africa. Compared to current conditions, these anomalies would have increased westerly air flow into southern Europe; this flow in turn would have increased orographic precipitation and thus produced cooler and moister summers at low to moderate elevations. The large increases in average July temperature reconstructed for high elevations might also be explained by more frequent incursions of moist air into the central European mountains, because at any given altitude the moist adiabatic lapse rate would then apply for a greater proportion of the growing season (*29*). This effect could conceivably have lowered the mean environmental lapse rate in summer by as much as 1°C km^{-1}, enough to produce the strong differential heating suggested by the results in Fig. 3.

REFERENCES AND NOTES

1. B. Huntley and H. J. B. Birks, *An Atlas of Past and Present Pollen Maps for Europe: 0–13,000 Years Ago* (Cambridge Univ. Press, Cambridge, 1983).
2. G. M. Peterson, thesis, University of Wisconsin–Madison (1983); J. C. Bernabo and T. Webb III, *Quat. Res. (N.Y.)* **8**, 64 (1977); M. Ralska-Jasiewiczowa, *New Phytol.* **94**, 133 (1983).
3. T. Webb III, *Vegetatio* **67**, 75 (1986).
4. I. C. Prentice, *Progr. Phys. Geogr.* **7**, 273 (1983).
5. S. Howe and T. Webb III, in *Fifth Conference on Probability and Statistics* (American Meteorological Society, Boston, 1977), pp. 152–157.
6. ——, *Quat. Sci. Rev.* **2**, 17 (1983).
7. P. J. Bartlein, T. Webb III, E. C. Fleri, *Quat. Res. (N.Y.)* **22**, 361 (1984).
8. P. J. Bartlein and T. Webb III, *Syllogeus* **55**, 301 (1985).
9. T. Webb III and R. A. Bryson, *Quat. Res. (N.Y.)* **2**, 70 (1972).
10. J. E. Kutzbach and P. J. Guetter, *J. Atmos. Sci.* **43**, 1726 (1986).
11. T. Webb III, P. J. Bartlein, J. E. Kutzbach, in *North America and Adjacent Oceans During the Last Deglaciation*, W. F. Ruddiman and H. E. Wright, Jr., Eds., vol. K-3 of *The Geology of North America* (Geological Society of America, Boulder, 1987), pp. 447–462.
12. B. Huntley and I. C. Prentice, in *Global Climates*, COHMAP Members, J. E. Kutzbach, W. A. Ruddiman, F. A. Street-Perrott, T. Webb III, H. E. Wright, Jr., Eds. (Univ. of Minnesota Press, Minneapolis, in press).
13. B. Huntley, in *Vegetation History*, B. Huntley and T. Webb III, Eds. (Kluwer, Dordrecht, in press).
14. ——, unpublished discriminant analysis; results (B.H.) show that groups of surface samples classified on the basis of their quantitative pollen composition can be discriminated with simple meteorological data for their localities.
15. COHMAP Project Members, *Science*, in press.
16. In this study, the maximally predictive subset among all possible subsets of the pollen variables was chosen as the subset with the lowest value of Mallows' C_p, given by:

$$C_p = \frac{SSE_p}{s^2} - (N - 2p)$$

where p is the number of variables in the model including the intercept, N is the number of observations, SSE_p is the sum-of-squares error for a model with p variables, and s^2 is the mean square error for the full model. This statistic quantifies the trade-off between increasing R^2 and decreasing prediction accuracy as the number of variables is increased. See S. Weisberg, *Applied Linear Regression* (Wiley, New York, ed. 2, 1985).
17. G. M. Peterson, *Quat. Sci. Rev.* **2**, 281 (1984); I. C. Prentice, *J. Biogeogr.* **10**, 441 (1983).
18. F. Steinhauser, *Climatic Atlas of Europe* (World Meteorological Organisation, Geneva, 1970), vol. 1.
19. J. T. Overpeck, T. Webb, III, I. C. Prentice, *Quat. Res. (N.Y.)* **23**, 87 (1985).
20. Initial boundaries that were based on the provenance of the modern analog samples were progressively adjusted until reconstructed temperatures on either side of any boundary were minimally affected by further change. The discrepancy between the alternative reconstructions for sites near the final boundaries was generally <0.5°C, but discrepancies of ≃2°C occurred in northernmost France and in a narrow zone on the steep temperature gradient across the Scandes. The remaining uncertainty in placing the boundaries means that errors in the reconstructed temperatures can be somewhat larger than is implied by the standard errors for the individual regression equations (Table 2), especially near the boundaries and in areas of high relief.
21. A reduced, mid-Holocene latitudinal gradient of summer temperature was also reported by Grichuk [M. P. Grichuk, in *Golotsen*, M. I. Neishtadt, Ed. (Idz-vo Nauka, Moscow, 1969), pp. 41–57] on the basis of an indicator-species method applied to a much smaller number of sites.
22. Guiot [J. Guiot, *Quat. Res. (N.Y.)* **28**, 100 (1987)], using a different form of the transfer function method, also found mid-Holocene July temperature anomalies of ≃5°C at high elevation sites in southern France.
23. J. Iversen, *Dan. Geol. Unders. Afh. Raekke 5* **7C**, 1 (1973).
24. J. Imbrie and J. Z. Imbrie, *Science* **207**, 943 (1980); J. D. Hays, J. Imbrie, N. J. Shackleton, *ibid.* **194**, 1121 (1976).
25. J. C. Ritchie, L. C. Cwynar, R. W. Spear, *Nature* **305**, 126 (1983).
26. J. E. Kutzbach, *Science* **214**, 59 (1981); M. Rossignol-Strick, *Nature* **304**, 46 (1983); J. E. Kutzbach and F. A. Street-Perrott, *ibid.* **317**, 130 (1985).
27. J. E. Kutzbach and P. J. Guetter, in *Milankovitch and Climate*, A. Berger, J. Imbrie, J. Hays, G. Kukla, B. Saltzman, Eds. (Reidel, Dordrecht, 1984), part 2, pp. 801–820.
28. ——, *Ann. Glaciol.* **5**, 85 (1984).
29. The moist adiabatic lapse rate is less than the dry adiabatic lapse rate because of the release of latent heat as water vapor in the moist air condenses during the cooling, which in turn results from expansion as the pressure of the body of air declines.

30. Natural Environment Research Council grant GR3/2877 and U.S. Department of Energy (DOE) grant DE-AC02-79-EV 10097 supported the data compilation; a University of Southampton Hartley Fellowship (to I.C.P.) and DOE grant DE-AC02-79-EV 10097 supported the climatic reconstruction. We thank H. J. B. Birks for his part in the development of the database; COHMAP project members at large for discussions throughout the project; and especially P. J. Bartlein, J. E. Kutzbach, and T. Webb III for encouragement and creative input. T. C. Atkinson, P. J. Bartlein, K. D. Bennett, J. C. Ritchie, J. Turner, W. A. Watts, and T. Webb III critically read earlier drafts.

2 February 1988; accepted 7 June 1988

The Titan −1:0 Nodal Bending Wave in Saturn's Ring C

PAUL A. ROSEN AND JACK J. LISSAUER*

The most prominent oscillatory feature observed in the Voyager 1 radio occultation of Saturn's rings is identified as a one-armed spiral bending wave excited by Titan's −1:0 nodal inner vertical resonance. Ring particles in a bending wave move in coherently inclined orbits, warping the local mean plane of the rings. The Titan −1:0 wave is the only known bending wave that propagates outward, away from Saturn, and the only spiral wave yet observed in which the wave pattern rotates opposite to the orbital direction of the ring particles. It is also the first bending wave identified in ring C. Modeling the observed feature with existing bending wave theory gives a surface mass density of ~0.4 g/cm² outside the wave region and a local ring thickness of ≲5 meters, and suggests that surface mass density is not constant in the wave region.

The Voyager 1 radio occultation profiles of Saturn's rings contain numerous wave-like features (*1*). We present strong evidence that the most prominent, previously unidentified, wave is a one-armed spiral bending wave excited by the gravitational potential of the satellite Titan at its −1:0 nodal inner vertical resonance (IVR) (*2*). Bending waves form when the periodic out-of-plane perturbations by a satellite in an inclined orbit and the self-gravity of the ring disk force particles near a resonance into locally coherent vertical oscillations, warping the plane of the rings into a corrugated spiral pattern (*3, 4*). A one-armed spiral bending wave arises at a nodal resonance, where the satellite perturbations act with a periodicity equal to that of the nodal regression rate of the ring particles. The wave propagates outward, away from Saturn. Its spiral pattern winds in a "leading" sense, that is, along the direction of motion of the particles; the pattern rotates, however, in a retrograde direction, against the particles' motion.

The Titan −1:0 nodal bending wave is

P. A. Rosen, Center for Radar Astronomy, Stanford Electronics Laboratories, Stanford University, Stanford, CA 94305-4055.
J. J. Lissauer, Astronomy Program, Department of Earth and Space Sciences, State University of New York, Stony Brook, NY 11794-2100.

*Alfred P. Sloan Research Fellow.

the first wave of this type to be identified. Among observed spiral structures in disks, including galaxies, it is the only known example of a leading wave, and of retrograde motion of the wave pattern. Of the five bending waves identified in Saturn's rings (*4, 5*), it is the only one-armed spiral, the only outwardly propagating wave, and the only wave located in ring C.

Figure 1 shows optical depth τ measured at 3.6 cm wavelength in the region of the Titan $-1{:}0$ IVR. The radio occultation signal-to-noise ratio at 200 m resolution in the wave region is high (*1*), allowing unambiguous measurement of each of the 28 observed wave oscillations. In this feature, wavelength decreases outward, away from Saturn. The W-shaped features and intervening "gap" fall outside the theoretical vertical resonance location, labeled as r_V in the figure, and appear to be an extension of the regular oscillations of the wave. Among Voyager data sets, the radio occultation profiles alone resolve this wave with high confidence (*6*).

Herein, we summarize the theory of nodal bending waves and relate the theory to the observations in Fig. 1, using the theoretical location, morphology, and wavelength dispersion to support our identification. Subsequently, we apply the theory to infer ring mass, viscosity, thickness, and particle sizes in the vicinity of the wave.

A bending wave can be excited where the periodicity of vertical forces exerted on ring particles by a moon in an inclined orbit is equal to an integer multiple of the particles' natural vertical oscillation period. The gravitational potential of a moon may be Fourier decomposed into the sum of terms having frequencies (*4*)

$$\omega = m\Omega_p = m\Omega_M + n\mu_M + p\kappa_M \qquad (1)$$

where the azimuthal symmetry number m is a non-negative integer, n and p are integers, and $\Omega(r)$, $\mu(r)$, and $\kappa(r)$ are, respectively, the orbital, vertical, and epicyclic (radial) frequencies of bodies orbiting near Saturn's equatorial plane at a mean distance r from the planet. The subscript M refers to those frequencies evaluated at the mean orbital radius of the perturbing moon. A bending waveform appears stationary in the frame rotating with the pattern speed, Ω_p. Vertical forcing terms occur only for odd n. For moons with small eccentricity e_M and inclination i_M, the strengths of these potential components are proportional to $e_M^{|p|} i_M^{|n|}$.

An IVR occurs at a location r_V where

$$m\Omega_p = m\Omega(r_V) - \mu(r_V) \qquad (2)$$

At a nodal IVR $m = 1$, so the forcing frequency equals the regression rate of the nodes of the orbits of particles. As Saturn is oblate, $\mu > \Omega$ in Saturn's equatorial plane (*7*), and Eq. 2 can only be satisfied for $\Omega_p < 0$ when $m = 1$. Thus, the pattern of a nodal wave must move in a retrograde sense relative to the orbits of the ring particles. Excluding retrograde satellites (Phoebe is very small and very far from the rings), the lowest order nodal IVR is a $-1{:}0$ resonance, which occurs for

$$\Omega_p = \Omega_M - \mu_M - \kappa_M \qquad (3)$$

Equations 2 and 3 give a location of the Titan $-1{:}0$ IVR of $r_V = 77515 \pm 13$ km (*8*), just inward of the feature in Fig. 1. No other strong known resonances of any type are within 300 km of this feature (*9, 10*). As Titan's orbit is nearly a closed ellipse, for which $\Omega = \mu = \kappa$, Ω_p is almost equal in magnitude to Titan's orbital frequency.

Self-gravity of the ring disk supplies a restoring force that enables bending waves to propagate away from resonance. The dispersion relation for linear free bending waves propagating in a region of constant surface mass density, σ, can be written as (*4*)

$$m^2[\Omega(r) - \Omega_p]^2 - \mu^2(r) = 2\pi G\sigma|k(r)| = \frac{4\pi^2 G\sigma}{\lambda(r)} \qquad (4)$$

where G is the gravitational constant, k is the radial wavenumber, and λ is the wavelength. Near an IVR, for $m > 1$, the left hand side (LHS) of Eq. 4 is a decreasing function of r, so bending waves are evanescent outside resonance and propagate inward; however, for an $m = 1$ resonance, the LHS of Eq. 4 increases with r because $\mu(r)$ decreases more rapidly than $\Omega(r)$. Therefore, nodal bending waves propagate outward, away from Saturn. Outward propagation implies the group velocity is positive and, from equation 23 of Shu *et al.* (*4*), it follows that nodal bending waves are leading.

The LHS of Eq. 4 varies slowly with r for $m = 1$, so nodal bending waves have long wavelengths (*11*). Equation 4 may be linearized to give the wavelength variation near the Titan $-1{:}0$ IVR:

$$\lambda(r) = 209\,\frac{\sigma_1}{r - r_V} \qquad (5)$$

where σ_1 is the surface mass density in the region of the resonance in units of g/cm^2 whereas r, r_V, and λ are in kilometers.

An explicit formula for the Titan nodal bending wave height profile is given by

$$Z(r) = \frac{|A_V|}{\pi^{1/2}} \times \mathrm{Re}\left[e^{i(\Phi_V + \pi/4)} e^{i\xi^2} \int_{-\infty}^{\xi} e^{-i\eta^2}\, d\eta\right] \qquad (6)$$

where Re denotes the real part and

$$\xi = 0.123\,\frac{r - r_V}{\sigma_1^{1/2}} \qquad (7)$$

with $r - r_V$ measured in kilometers. The

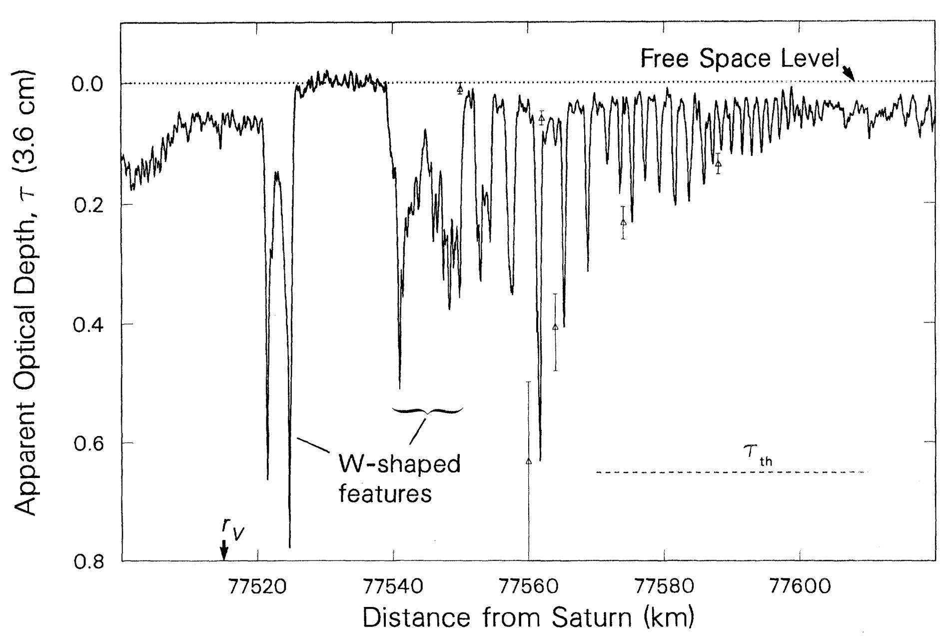

Fig. 1. Voyager 1 radio occultation data, showing wave-like oscillations of apparent normal radio (3.6 cm) optical depth τ, at 200 m resolution, that result from a bending wave excited by the Titan $-1{:}0$ nodal inner vertical resonance located at $r_V = 77515 \pm 13$ km (standard error). In the highly oblique geometry of the radio occultation, the apparent optical depth is greatly affected by slope variations of the disk (*14*), creating such unusual features as the apparent gap near resonance flanked by W-shaped features. Measurement errors increase as τ approaches the threshold τ_{th}, beyond which the signal is indistinguishable from the noise. Error bars shown at selected levels of τ are 70% confidence intervals. The shortest wavelengths are nearly five times the data resolution.

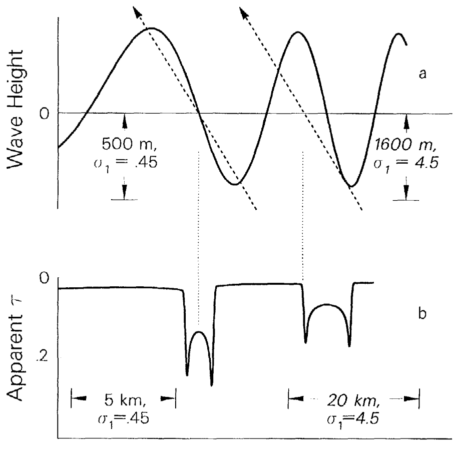

Fig. 2. (**a**) Oblique incidence of the radio signal (dashed lines) on the warped disk in the propagation region of a bending wave. The ring is presumed to have finite thickness that is constant in the vertical direction. Apparent τ (**b**) is proportional to the total path length over which the radio signal encounters the wave (*14*). The W-shaped morphology near r_V in the observation (Fig. 1) is well modeled by a ring with $\sigma_1 = 4.5$ and an amplitude about ten times greater than the theoretically derived value (Eq. 8). Scale indicators in italics on the right apply to this model. The same morphology is obtained with $\sigma_1 = 0.45$ and the theoretical wave amplitude (scale on left), however the wavelength scale then fails to match the observations.

amplitude of the excited bending wave is (*12*)

$$|A_V| = \frac{334}{\sigma_1^{1/2}} \text{ meters} \qquad (8)$$

The phase of the wave at the location of the radio occultation observation is $\Phi_V = 174°$ (*13*). In the following, we show that the observations are consistent with these theoretical properties.

A radio signal passing obliquely through a planetary ring measures slant optical depth, $\tau_q = \tau/\sin\theta$, where τ is the normal optical depth and θ is the obliquity of the occultation ray with respect to the local ring plane. For a flat ring, $\theta = \theta_0$ is constant and normal optical depth can be inferred from τ_q. In a bending wave, variations in θ that are due to the warping of the disk produce local oscillations in τ_q that can mimic oscillations in τ (*14*). Moreover, if the local slope of the disk exceeds θ_0, the radio signal passes through the warped disk more than once, and features in observed (apparent) optical depth can be quite distinctive. "Apparent optical depth" plotted in Fig. 1, gives τ computed from τ_q assuming $\theta = \theta_0$, and offers ample evidence (28 cycles) of such signatures. The W-shaped features and intermediate "gap" in the region 77520–77550 km are unique in the radio data (*1*), yet are modeled readily by multiple passages of the signal through a nodal bending wave with steep slope. Their presence between the theoretical location r_V and the outwardly propagating wave is strong evidence that the entire observation is the signature of a one-armed spiral bending wave.

Figure 2 shows the mapping of wave height $Z(r)$ (Eq. 6) to apparent τ for the first few cycles of a model wave propagating in a region with $\sigma_1 = 0.45$. This value of σ was chosen specifically to bring the model and observed morphologies of apparent τ into best agreement. Comparison of Figs. 1 and 2 illustrates the striking similarity between their shapes in the first part of the wave; however, the radial scale of the model W-shaped features is far smaller than the observed scale. It is not possible to model the correct scale and shape simultaneously with the theoretical relationship between amplitude $|A_V|$ and surface mass density σ (Eq. 8). However, treating $|A_V|$ and σ as independent free parameters in Eqs. 6 and 7 allows us to match the observations. We obtain the same morphology of apparent τ and the proper radial scale if σ and $|A_V|$ are taken to be 4.5 g/cm^2 and 1600 m, respectively. The italicized scale indicators in Fig. 2 allow reinterpretation of the curves for these parameter values. As the derivation of Eq. 6 assumes constant surface mass density (*4*), a rapid change of σ in the first few cycles, as suggested by the dispersion analysis below, could affect the values of these quantities.

The regularity of the remainder of the wave suggests a rapid outward decrease in wave slopes at $r \simeq 77555$ km such that multiple passages do not occur outside the W-shaped features (*15*). (In the following, we call the region $r \gtrsim 77555$ km either the "far-wave" or the "regular" region.) In such a low-slope region, the radial wavelengths of the height profile can be approximated by a measurement of the separation between consecutive maxima or minima of apparent τ. Except where $r < 77555$ km, the wavelengths plotted in Fig. 3 (upper right) are measured in this way. We estimate $\sigma_1 \sim 0.3$ and a resonance location of 77542 km from a least-squares fit of Eq. 5 to these $\lambda(r)$ measurements. The resonance location estimate agrees poorly with the theoretical position, $r_V = 77515 \pm 13$ km.

The analysis of the W-shaped features suggests that the value of σ there is greater than that given by the above dispersion analysis in the far-wave region. In addition, an enhancement of σ within the wave is

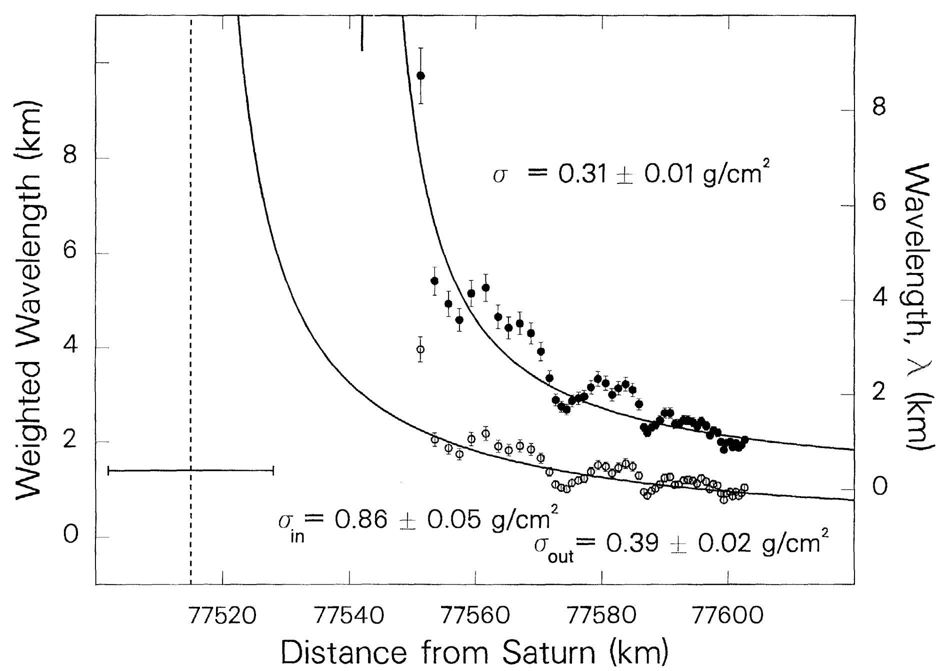

Fig. 3. Wavelength λ (solid circles, right vertical axis) measured from the apparent optical depth profile (Fig. 1). The associated curve is a fit of Eq. 5 to λ assuming constant surface mass density, σ. The vertical dashed line marks the theoretical resonance location, r_V. The accompanying horizontal error bar delimits its ± 13 km uncertainty (*8*). The fitted resonance location is 77542 ± 1 km (dark bar on upper scale), which is significantly exterior to r_V. The estimate of σ is given to the right of the curve. Open circles (left vertical axis) are wavelengths weighted by a linearly decreasing function $\sigma(r)/\sigma_{out}$ chosen to best model the variation of surface density $\sigma(r)$ in the wave region when the resonance location is fixed at r_V. The associated curve represents the theoretical dispersion (Eq. 5) for this $\sigma(r)$. The quantity σ_{out} is the surface density at the location of the last estimated wavelength, $r = 77603$ km; σ_{in} is the surface density at the first wavelength, $r = 77551$ km. The cause of the quasi-periodic wavelength variation about the fitted curves is unknown. All error bars and derived uncertainties are standard errors.

consistent with the Voyager 2 Photopolarimeter (PPS) observation, which shows optical depth τ_{PPS} increasing toward resonance in the regular region, with a maximum in the vicinity of the "W's". Variation of σ in the regular region could account for the discrepancy between the above derived resonance location and r_V. Therefore, we consider a simple model for the variation in σ that can relieve the disagreement in a consistent manner. In Eq. 5, we assume σ decreases linearly with increasing radius (*16*), and fit the values of σ at the locations of the first and last clearly observed cycles, denoted σ_{in} and σ_{out} respectively, with the resonance location fixed at r_V. Wavelengths weighted by the fitted variation $\sigma(r)/\sigma_{out}$ are plotted in Fig. 3. The fit gives $\sigma_{in} = 0.86$ g/cm^2, decreasing to an ambient value $\sigma_{out} = 0.39$ g/cm^2 as the wave dies out. This range of σ values is consistent with independent density estimates from dispersion analysis of the nearby Mimas 4:1 density wave (*10*), further strengthening our identification of the nodal bending wave.

The first weighted wavelength estimate in Fig. 3 is well out of line with the remaining estimates, suggesting that the true surface density variation is probably not linear. More severe mass accumulation occurring near resonance is consistent with the large value of σ necessary to model the width and separation of the W-shaped features in Fig. 2. Mass buildup in propagation regions of density waves is observed commonly in Saturn's rings, and may be due to nonlinear viscous "dredging" near resonance (*17*). Similar processes may be at work here.

Linear viscous damping causes the amplitude of a bending wave to decrease according to (*4*)

$$A(r) \approx A_V \, e^{-|(r - r_V)/l_D|^3} \tag{9}$$

where l_D is a measure of the damping length of the wave. The viscosity of the ring in the Titan $-1:0$ wave region is then

$$\nu = 4.76 \times 10^5 \left(\frac{\sigma_1}{l_D}\right)^3 \frac{\text{cm}^2}{\text{sec}} \tag{10}$$

where ν is assumed constant and l_D is in kilometers. The observations indicate that considerable damping occurs near the beginning of the wavetrain; this cannot be the result of linear viscous damping of the form given by Eq. 9, as the required damping length would terminate the wave well before the 28 cycles observed. Similar problems occurred in an attempt to fit the profile of the Mimas 5:3 bending wave with a constant ν (*14*). The slope of the Titan wave is large enough that nonlinear damping may be important; other damping mechanisms may also play a role (*18*). We therefore can only estimate an upper limit to the portion of the damping due to viscosity, implying an upper bound on ν. The extent of the Titan $-1:0$ wave implies $l_D \gtrsim 50$ km; taking $\sigma = 0.4$ g/cm^2 gives $\nu \lesssim 0.24$ cm^2/s. The corresponding ring scale height is $\lesssim 2.6$ m (*19*).

In conclusion, on the basis of its location, morphology, and wavelength dispersion, we attribute the most prominent oscillatory feature in the radio occultation data of Saturn's rings to a spiral bending wave excited by the Titan $-1:0$ nodal inner vertical resonance. Analysis of the well-behaved far-wave oscillations gives a surface mass density $\sigma = 0.4 \pm 0.1$ g/cm^2 at the outer extremity of the wave region (*20*), increasing toward resonance within the wavetrain. This value of σ is only 1% of that in ring A, even though the optical depth of the region is about 10% as large as in ring A. We therefore conclude that particles in ring C are smaller (or less dense) than those in ring A, in agreement with radio scattering and extinction measurements (*21*) and other observations (*22*). From the persistence of the wave for over 28 cycles we infer that the scale height of the ring does not exceed 2 to 3 m in this region, that is, 70% of the ring material lies within a layer which is locally $\lesssim 5$ m thick. Preliminary model τ profiles, computed with linear bending wave theory and constant surface mass density, exhibit striking similarities to the observations, but fail to describe the entire wavetrain consistently. Models computed with enhanced surface mass density near resonance agree better with the observations but require a larger amplitude for the first two cycles than is predicted by the theory. The disagreement between theory and observation is likely the result of substantial, rapid variations of surface mass density near resonance and more gentle variations in the far-wave region. Further effort will be required to understand more completely the detailed behavior of this wave.

REFERENCES AND NOTES

1. E. A. Marouf, G. L. Tyler, P. A. Rosen, *Icarus* **68**, 120 (1986).
2. Inner vertical resonances are conventionally labeled $m + n + p : m - 1$, denoting the ratio of the orbital period of the moon to that of the ring particles at resonance if $\Omega = \kappa = \mu$, that is, if orbits were closed (Eqs. 1 and 2). As orbits are nearly closed, this ratio approximately holds for all but nodal resonances, whose existence depends on the nonclosure of orbits.
3. C. Hunter and A. Toomre [*Astrophys. J.* **155**, 747 (1969)] developed much of linear bending wave theory in a galactic context.
4. F. H. Shu, J. N. Cuzzi, J. J. Lissauer, *Icarus* **53**, 185 (1983).
5. J. J. Lissauer, *ibid.* **62**, 433 (1985).
6. Other observations in this region include Voyager images [B. A. Smith *et al.*, *Science* **212**, 163 (1981)] and Voyager 2 Ultraviolet (UVS) and Photopolarimeter (PPS) occultation observations [B. S. Sandel *et al.*, *ibid.* **215**, 548 (1982); A. L. Lane *et al.*, *ibid.*, p. 537]; however, because the ring opening at Voyager 1 encounter was only 6°, the radio occultation experiment was particularly well suited to probing bending waves, whose slope variations relative to the propagation direction of the radio beam map to strong signal variations in the observed profiles (*14*).
7. F. H. Shu, in *Planetary Rings*, R. Greenberg and A. Brahic, Eds. (Univ. of Arizona Press, Tucson, 1984), pp. 513–561.
8. This location is based on Saturn's mass and revised values of Saturn's gravitational harmonics given by P. D. Nicholson and C. C. Porco (*J. Geophys. Res.*, in press). Their solution for the gravitational harmonics is dependent in part on the identification of the nearby Titan 1:0 apsidal resonance at 77852 km. The quoted uncertainty of r_V comes from their work and is an estimate of the standard error.
9. J. J. Lissauer and J. N. Cuzzi, *Astron. J.* **87**, 1051 (1982).
10. P. A. Rosen, thesis, Stanford University (1988).
11. An analogous situation occurs for apsidal spiral density waves [J. N. Cuzzi, J. J. Lissauer, F. H. Shu, *Nature* **292**, 703 (1981)], the in-plane cousins of nodal bending waves. The relatively long observed wavelengths of the feature presented herein, together with its proximity to the Titan 1:0 apsidal resonance, first suggested to us that it was an $m = 1$ spiral wave.
12. The numerical constant in Eq. 8 is obtained in part from equations A23, a and b, of Shu (7), in which there are three misprints. The correct version of those equations is

$$f_M = -\frac{3GMe_M \sin i_M}{4a_M^2} e^{i(\kappa_M t_0 - \pi/2)} B_{5/2}^{(-)} \tag{11}$$

and

$$B_{5/2}^{(-)} = b_{5/2}^{(m)} - \frac{r_V}{2a_M}\left[\left(1 + \frac{2\Omega_M}{\kappa_M}\right) b_{5/2}^{(m-1)} + \left(1 - \frac{2\Omega_M}{\kappa_M}\right) b_{5/2}^{(m+1)}\right] \tag{12}$$

where $b_{5/2}^{(j)}$ (r/a_M) are Laplace coefficients [D. Brouwer and G. M. Clemence, *Methods of Celestial Mechanics* (Academic Press, New York, 1961)], M is the mass of Titan, and a_M is the mean orbital radius of Titan. Other terms are defined in the text.
13. The phase of the wave may be computed from

$$\Phi_M = \Omega_p \, t - \theta + \kappa_M t_0 + \frac{3\pi}{4} \tag{13}$$

where here θ is the longitude of the wave observed at time t. Titan's periapse passage occurs at time t_0 while its ascending node crossing occurs at time $t = 0$.
14. D. L. Gresh, P. A. Rosen, G. L. Tyler, J. J. Lissauer, *Icarus* **68**, 481 (1986).
15. Multiple passages of the radio signal in the region outside the W-shaped features would modulate the envelope of apparent τ in a way similar to what is observed. However, this would be accompanied by periodic phase reversals in the oscillations, creating distinctly irregular behavior which is not observed (*10*). In addition, variability in surface density could result in modulation.
16. Typically, background σ is determined from a measurement of background τ by assuming σ/τ is constant. However, it is difficult to estimate the background variations of radio τ because of the mapping effect of the obliquity in the wave region.
17. F. H. Shu, H. C. Dones, J. J. Lissauer, C. Yuan, J. N. Cuzzi, *Astrophys. J.* **299**, 542 (1985).
18. J. J. Lissauer, F. H. Shu, J. N. Cuzzi, in *Planetary Rings*, A. Brahic, Ed., Proceedings IAU Symp. No. 75 (Centre National d'Études Spatiales, Toulouse, France, 1984), pp. 385–392.
19. P. Goldreich and S. Tremaine, *Icarus* **34**, 227 (1978).
20. The error bar for σ reflects the sensitivity of the fitting method that assumes linear variations of σ in the far-wave region to the assumed resonance location, which is uncertain by ± 13 km standard error (*8*).

21. H. A. Zebker, E. A. Marouf, G. L. Tyler, *Icarus* **64**, 531 (1985).
22. L. W. Esposito *et al.*, *Science* **222**, 57 (1983); M. R. Showalter and P. D. Nicholson, in preparation.
23. We thank G. L. Tyler for particularly careful review of this paper, and L. Dones, D. Gresh, E. Marouf, R. Simpson, F. Shu, J. Cuzzi, P. Nicholson, and C. Porco for helpful discussions. This work was supported in part under JPL contract 953618 and NASA grant NAGW 1107.

29 February 1988; accepted 24 May 1988

Role of the Glutathione Redox Cycle in Acquired and de Novo Multidrug Resistance

ROBERT A. KRAMER, JEHANE ZAKHER, GEORGE KIM

Drug resistance represents a major obstacle to successful cancer chemotherapy. However, the specific biochemical mechanisms responsible for clinical drug resistance are unknown. In these studies resistance to the antitumor agent adriamycin was found to involve two mechanisms, one that decreased drug accumulation by the P170 mechanism and another that altered the glutathione redox cycle, an important pathway in the detoxification of reactive oxygen. This dual mechanism of drug resistance was demonstrated in cell lines that had acquired the multidrug-resistant phenotype and in human colorectal cancer cells with de novo resistance. These studies support a model of acquired and de novo multidrug resistance that includes alterations in both drug accumulation and the glutathione redox cycle.

MULTIDRUG RESISTANCE (MDR) describes a problematic form of resistance in which tumor cells that become refractory to treatment with one drug develop cross resistance to a variety of agents that include antitumor antibiotics such as the anthracyclines, vinca alkaloids, and epidophyllotoxins (*1*). A characteristic feature of MDR cells is a decrease in drug accumulation that is associated with the increased production of a membrane glycoprotein termed P170 (*2*). This protein binds a drug and facilitates efflux by an energy-dependent process (*3*). The gene coding for P170 (*mdr*-1) has been cloned (*4*) and was expressed at levels that are proportional to the degree of resistance in several multidrug-resistant cell lines (*5*). P170 is also expressed in human tumor tissues including tumors of the colon, adrenal, ovary, and breast (*6*). Although the increased expression of P170 is an important component of acquired MDR, it is unlikely to be the sole mechanism of resistance for the broad spectrum of compounds that encompass MDR (7). In primary or de novo forms of resistance, for example, a clear relation between the expression of P170 and tumor response to chemotherapy has not been established (*6, 7*).

Evidence of a role for "non–P170-mediated" mechanisms of resistance in MDR cells was demonstrated in the following studies, in which we used the Ca^{2+} channel antagonist verapamil (Ver) (Table 1 and Fig. 1). Verapamil was previously shown to bind to the active site of P170, thereby inhibiting drug efflux (*8*). However, we observed that Ver treatment did not confer full sensitivity to the anthracycline adriamycin (Adr) in MDR human breast carcinoma (MCF/Adr) and murine leukemia (P388/Adr) cell lines. These cells display the MDR phenotype of cross-resistance, decreased drug accumulation, and overexpression of the *mdr*-1 gene (*9, 10*). The MCF/Adr and P388/Adr cells were, respectively, 94 and 37 times as resistant to Adr as drug-sensitive cell lines (Table 1). Treatment with Ver (10 μg/ml) partially restored Adr sensitivity, decreasing the 50% inhibitory concentration (IC_{50}) value for Adr by about seven times in each cell line. This dose of Ver produced a sixfold increase in the steady-state concentration of [^{3}H]-daunomycin (Fig. 1), whereas MCF/Adr cells accumulated 1/30 as much [^{3}H]daunomycin as the parent cell line. The maximum effect achieved with Ver (50 μg/ml) resulted in a ninefold increase in drug uptake and in a corresponding decrease in the IC_{50} value to one-ninth that of Adr. These studies demonstrate that altered drug accumulation alone cannot account for Adr resistance in MCF/Adr and P388/Adr cell lines.

Studies of Batist *et al.* (*11*) showed that a 45-fold increase in glutathione *S*-transferase (GST) activity occurs in MCF/Adr cells. The GSTs are a multigene family of isoenzymes that catalyze the conjugation of glutathione (GSH) to a variety of electrophilic compounds as the first step in a detoxification pathway leading to mercapturic acid formation (*12*). However, MCF/Adr cells express a specific anionic isoenzyme of GST that presumably possessed high levels of intrinsic peroxidase activity (*11*). Peroxidase activity mediated by GST, otherwise known as non–selenium-dependent glutathione peroxidase (GSH-Px) (*12*), was believed to account for the decreased formation of hydroxyl radicals observed in MCF/Adr cells exposed to Adr (*13, 14*). The generation of oxyradicals produced by the redox cycling of the quinone moiety of Adr is believed to contribute to the antitumor activity of this and related compounds (*15*). Therefore, it is

Joint Center for Radiation Therapy, Harvard Medical School, Boston, MA 02115.

Table 1. Enhancement of Adr cytotoxicity by BSO and Ver. The IC_{50} values were calculated as the concentration of Adr that inhibits day 4 [^{3}H]thymidine incorporation by 50% in human breast (MCF and MCF/Adr) and colon cancer cells (MIP-101 and DLD-1), and inhibits growth at 72 hours by 50% in P388 cells. Log phase monolayer cultures of human breast or colon cells, and suspensions of P388 cells were incubated with Adr for 3 hours. Cells were washed free of drugs and allowed to grow in RPMI 1640 medium supplemented with 10% fetal bovine serum. After 72 hours, P388 cell growth was assessed by counting (Coulter Electronics), and MCF and colon cell growth was measured by incorporation of [^{3}H]thymidine (6.7 Ci/m*M*; New England Nuclear). [^{3}H]Thymidine was incubated with cells for 24 hours and incorporation into trichloroacetic acid–precipitable material was determined (*25*). BSO treatment was 200 μ*M* for MCF and colon cells and 10 μ*M* for P388 cells, and was administered for 24 hours before the Adr. This treatment decreased GSH concentrations in the various cell lines by 75 to 90% without affecting cell doubling times. DOP is defined as the degree of potentiation calculated by IC_{50} control/IC_{50} treated. Ver was added simultaneously with Adr at doses of 10 μg/ml in MCF and colon cells, and 5 μg/ml in P388. Values are the means of four to six experiments, with SE less than 10% of the reported values.

Source	IC_{50} values for Adr (μ*M*)						
	Control	BSO	(DOP)	Ver	(DOP)	BSO/Ver	(DOP)
Cell lines							
MCF	0.16	0.13	(1)	0.08	(2)	0.08	(2)
MCF/Adr	15.0	3.40	(4)	2.30	(7)	0.15	(100)
P388	0.01	0.01	(1)	0.03	(0.3)	0.02	(0.5)
P388/Adr	0.37	0.18	(2)	0.05	(8)	0.01	(37)
Colon lines							
DLD-1	0.20	0.05	(4)	0.10	(2)	0.02	(10)
MIP-101	2.00	0.70	(3)	0.20	(10)	0.08	(25)